

Multi-line (sub)millimetre observations of the high-mass proto cluster IRAS 05358+3543[★]

S. Leurini^{1,2}, H. Beuther³, P. Schilke¹, F. Wyrowski¹, Q. Zhang⁴, and K. M. Menten¹

¹ Max-Planck-Institut für Radioastronomie, Auf dem Hügel 69, 53121 Bonn, Germany

² ESO, Karl-Schwarzschild Strasse 2, 85748 Garching-bei-München, Germany
e-mail: sleurini@eso.org

³ Max-Planck-Institut für Astronomie, Königstuhl 17, 69117 Heidelberg, Germany

⁴ Harvard-Smithsonian Center for Astrophysics, 60 Garden Street, Cambridge, MA 02138, USA

Received 30 May 2007 / Accepted 20 September 2007

ABSTRACT

Context. Since most high- and intermediate-mass protostars are at great distance and form in clusters, high linear resolution observations are needed to investigate their physical properties.

Aims. To study the gas in the innermost region around the protostars in the proto-cluster IRAS 05358+3543, we observed the source in several transitions of methanol and other molecular species with the Plateau de Bure Interferometer and the Submillimeter Array, reaching a linear resolution of 1100 AU.

Methods. We determine the kinetic temperature of the gas around the protostars through an LVG and LTE analysis of their molecular emission; the column densities of CH₃OH, CH₃CN and SO₂ are also derived. Constraints on the density of the gas are estimated for two of the protostellar cores.

Results. We find that the dust condensations are in various evolutionary stages. The powerhouse of the cluster, mm1a, harbours a hot core with $T \sim 220$ ($75 < T < 330$) K. A double-peaked profile is detected in several transitions toward mm1a, and we found a velocity gradient along a linear structure which could be perpendicular to one of the outflows from the vicinity of mm1a. Since the size of the double-peaked emission is less than 1100 AU, we suggest that mm1a might host a massive circumstellar disk. The other sources are in earlier stages of star formation. The least active source, mm3, could be a starless massive core, since it is cold ($T < 20$ K), with a large reservoir of accreting material ($M \sim 19 M_{\odot}$), but no molecular emission peaks on it.

Key words. stars: formation – stars: early type – stars: individual: IRAS 05358+3543 – ISM: molecules

1. Introduction

The last decade has seen significant progress in the understanding of how high-mass stars form. Large samples of massive young stellar objects (YSOs) were studied with single-dish telescopes, to investigate their physical properties through the analysis of their (sub)mm continuum and molecular emission (e.g., Molinari et al. 1996, 1998, 2000; Walsh et al. 1997, 1998, 1999; Hatchell et al. 2000; Zhang et al. 2001, 2005; Sridharan et al. 2002; Beuther et al. 2002b,c; Faúndez et al. 2004; Williams et al. 2004, 2005). However, an intrinsic feature of high-mass stars is that they form in clusters, and that most of them are at large (several kpc) distances. Therefore, single-dish studies, as valuable as they are, lack the necessary spatial resolution to resolve single protostars and study the inner regions where high-mass star formation takes place. Interferometric observations started shedding light into the complex nature of high-mass star forming regions with the adequate spatial resolution (e.g., Cesaroni et al. 1997, 1999, 2005; Wyrowski et al. 1999; Beuther et al. 2002a, 2005; Hunter et al. 2006; Shepherd et al. 2000). However, the number of massive YSOs studied at high resolution is still too small to establish the general properties of the dense cores where massive stars form on a statistical base.

In this paper, we present an interferometric analysis of the high-mass star forming region IRAS 05358+3543 at (sub)mm wavelengths in several molecular transitions. IRAS 05358+3543 (also known in literature as S233IR) is part of a sample of 69 high-mass protostellar objects studied in great detail in recent years (Sridharan et al. 2002; Beuther et al. 2002b,c,d; Williams et al. 2004, 2005; Fuller et al. 2005). At a distance of 1.8 kpc (Snell et al. 1990), IRAS 05358+3543 has a bolometric luminosity of $6300 L_{\odot}$; strong high-mass star formation activity is evidenced by maser emission (see Menten 1991; Tofani et al. 1995; Minier et al. 2000) and outflow activity (Snell et al. 1990; Beuther et al. 2002a). Previous interferometric observations by Beuther et al. (2002a) resolved three dust condensations (mm1, mm2 and mm3) within an area of $9'' \times 4''$ ($\sim 17\,100 \times 7200$ AU), and revealed at least three outflows in CO and SiO, the most prominent of which is more than a parsec in length, and massive ($M > 10 M_{\odot}$). Two of the three identified outflows originate from the vicinity of mm1, which is probably the main powerhouse in the region.

To zoom in on the innermost region around the protostars, and study the physical properties of the individual potentially star-forming cores, we carried out a comprehensive program to observe the region at high spatial resolution with the Plateau de Bure Interferometer¹ at 97 GHz and 241 GHz, and the

[★] UV tables of interferometer maps plus IRAM 30-m map are only available in electronic form at the CDS via anonymous ftp to cdsarc.u-strasbg.fr (130.79.128.5) or via <http://cdsweb.u-strasbg.fr/cgi-bin/qcat?J/A+A/475/925>

¹ IRAM is supported by INSU/CNRS (France), MPG (Germany) and IGN (Spain).

Table 1. Positions of the four dust condensations in IRAS 05358+3543 (from Beuther et al. 2007a).

Source	RA [J2000]	Dec [J2000]
mm1a	05:39:13.08	35:45:51.3
mm1b	05:39:13.13	35:45:50.8
mm2a	05:39:12.76	35:45:51.3
mm3	05:39:12.50	35:45:54.9

Submillimeter Array² at 338 GHz. The new observations reach a resolution down to 0.6'', corresponding to ~ 1100 AU at the distance of the source. Beuther et al. (2007a) studied the continuum emission of this dataset. They identified four compact protostellar sources in the region; mm1 is resolved into two continuum peaks, mm1a and mm1b, with a projected linear separation of ~ 1700 AU. A mid-infrared source (Longmore et al. 2006), and a compact 3.6 cm continuum source (Beuther et al. 2007a) coincide with mm1a, which is also associated with the class II methanol masers detected by Minier et al. (2000). The previously identified source mm2 resolves into several sub-sources; however, only one of them (mm2a, according to the nomenclature used by Beuther et al. 2007a) is a protostellar source, while the others are probably caused by the outflows in the region. The third source mm3 remains a single compact core even at the highest spatial resolution. In Table 1, we report the positions of the four sources identified in the continuum emission by Beuther et al. (2007a).

In this paper, we discuss the spectral line observations complementing the continuum data discussed by Beuther et al. (2007a). In Sect. 2, the different observations are presented. In Sect. 3, we discuss our results, and analyse the extended emission of low excitation molecular transitions (Sect. 3.1), as well as the molecular spectra at the positions of the dust condensations (Sect. 3.2). Finally, in Sect. 4 we derive the physical parameters of the gas around the protostars from the analysis of their spectra. In the following sections, we use the term protostar for young massive stellar objects which are still accreting material from the surroundings, independently of whether they already started burning hydrogen or not.

2. Observations

2.1. Plateau de Bure Interferometer (PdBI)

IRAS 05358+3543 was observed with the IRAM Plateau de Bure Interferometer in two different frequency setups, in 2003 and 2005. A first frequency setup was performed in four tracks between January and October 2003 in the BC and D configurations of the array. Two observations, in January and October, were performed with only 5 antennas; on January 12th, 2003, the array was configured in a special BC combination. The 3 mm receivers were used in single-sided band mode and tuned to 96.6 GHz; the 1 mm receivers, in double-sided band mode, were tuned to 241.85 GHz (USB). At 3 mm, the $C^{34}S$ line and the torsionally excited $2_k \rightarrow 1_k$ CH_3OH quartet were covered using two correlator units of 80 MHz bandwidth. One 320 MHz unit was placed to obtain a continuum measurement at 3 mm. The $5_k \rightarrow 4_k$ $v_t = 0$ CH_3OH band, the $2_{1,1} \rightarrow 2_{1,2}$ HDO and the $5 \rightarrow 4$ SO_2 lines were observed with four units of 160 MHz

bandwidth, which were also used to obtain a continuum measurement at 1.3 mm. The same configuration of the correlator units allowed the observation of $13_k \rightarrow 12_k$ CH_3CN band in the LSB at 239 GHz. The observations were performed in the MOSAIC mode, with seven fields covering the whole source in a hexagonal pattern with a centre field (see Fig. 1).

The second frequency setup was observed on February 4th and February 7th, 2005, in the A and B configurations. The 3 mm receivers were used in single-side band mode and tuned again to 96.6 GHz, with the same configuration of the correlator described before. The 1 mm receivers, in double side-band mode, were tuned to 241.2 GHz (USB) with three 160 MHz units covering the $5_k \rightarrow 4_k$ $v_t = 1$ CH_3OH band.

Bandpass calibration was done with 0420-014, 3C 454.2 and NRAO150 for the BCD configuration, with 3C 84 for the AB data. NRAO150, 0528+134 and 3C 273 were used as flux calibrators of the BCD and AB data, respectively. Phase and amplitude calibration was done via observations of 0528+134, 0552+398, 0529+483 and J0418+380. Measured system temperatures were between 100 and 260 K in the 3.1 mm band for both setups. On February 4th, the system temperatures in the 1.2 mm receivers ranged between 240 and 420 K, with one receiver measuring system temperatures of 900 K. On February 7th, and during the observations of the first frequency setup, the system temperatures in the 1.2 mm bands were higher, between 400 and 1000 K, due to less favourable weather conditions.

For both frequency setups, the phase centre was $\alpha_{2000} = 05^h39^m13^s.07$, $\delta_{2000} = +35^\circ45'50''.5$, with $v_{LSR} = -17.6$ km s⁻¹. Details on the spectral resolutions, the synthesised beam sizes and the main spectral lines per frequency units are given in Table 2. For the AB configuration the baselines range between 30 and 400 m, for the BCD configuration between 20 and 320 m. Therefore, at 1.2 mm any source structure larger than 6'' is filtered out in the AB observations, and larger than 13'' in the BCD data.

The data calibration and the imaging were performed with the CLIC and MAPPING software³. For the PdBI and the SMA data, line free channels were averaged to produce continuum images, which were then subtracted from the line data in the visibility plane⁴.

2.2. Submillimeter Array

We observed IRAS 05358+3543 with the SMA on November 11th, 2004, at 348 GHz (865 μ m) in the compact configuration with seven antennas, and on January 15th, 2005, in the extended configuration again with seven antennas in the array. However, the data from one antenna in the extended configuration were unusable reducing it to six effective antennas for that configuration. Due to problems at the correlator during the observations in the extended configuration, the frequency of the $7 \rightarrow 6$ $C^{34}S$ line was not covered. However, the $7 \rightarrow 6$ $C^{34}S$ map was produced from the compact configuration data. The projected baselines ranged between 13 and 223 m. The short baseline cutoff implies that source structures $\geq 16''$ are filtered out by the observations. The phase centre of the observations was $\alpha_{2000} = 05^h39^m13^s.07$ and $\delta_{2000} = +35^\circ45'51''.2$

³ <http://www.iram.fr/IRAMFR/GILDAS>

² The Submillimeter Array is a joint project between the Smithsonian Astrophysical Observatory and the Academia Sinica Institute of Astronomy and Astrophysics and is funded by the Smithsonian Institution and the Academia Sinica.

⁴ The calibrated UV tables related to the PdBI and SMA observations are available in electronic form at the CDS. The integrated intensity map of the $5_0 \rightarrow 4_0$ $v_t = 0$ CH_3OH -A line with the 30 m IRAM is also available in electronic form at the CDS.

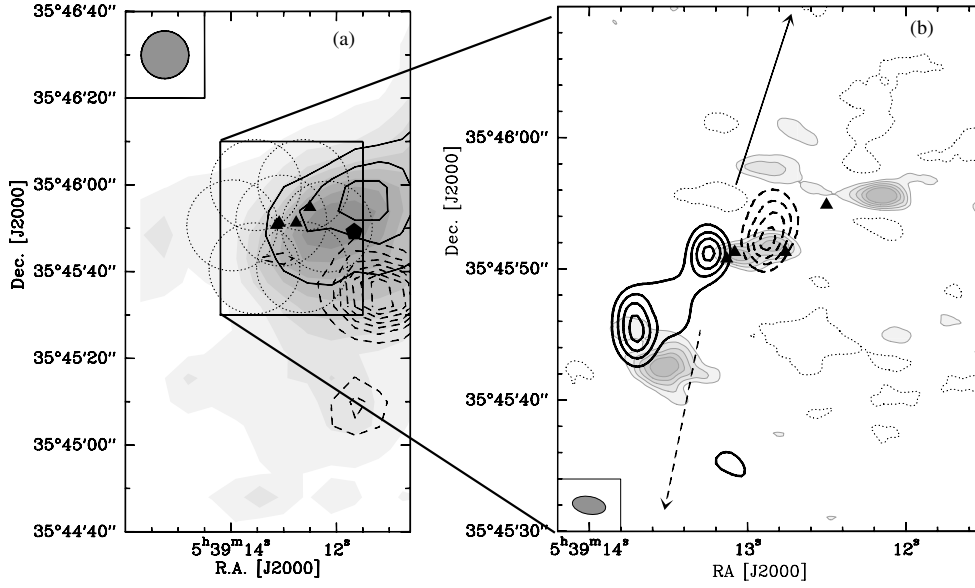


Fig. 1. **a)** In grey scale, the map of the integrated intensity of the $5_0 \rightarrow 4_0 v_t = 0$ $\text{CH}_3\text{OH-A}$ line with the 30 m IRAM telescope ($v = [-17, -16]$ km s^{-1} ; levels from $0.5 \text{ Jy beam}^{-1} \text{ km s}^{-1}$ in steps of 0.5). The dashed contours show the blue-shifted emission ($v = [-23, -20]$ km s^{-1} ; levels from $0.5 \text{ Jy beam}^{-1} \text{ km s}^{-1}$ in steps of 0.5); the solid lines the red-shifted emission ($v = [-14, -12]$ km s^{-1} ; levels from $1 \text{ Jy beam}^{-1} \text{ km s}^{-1}$ in steps of 0.5). The beam is indicated in the top left corner. The dotted circles outline the observed mosaic of seven fields. The pentagon locates the position of one of the H^{13}CO^+ peaks observed by Beuther et al. (2002a), which is the candidate centre for the outflow traced by CH_3OH . The solid lines outline the region shown in panel **b)**. **b)** In grey scale (and grey contours), the map of the integrated intensity of the $5_0 \rightarrow 4_0 v_t = 0$ $\text{CH}_3\text{OH-A}$ line with the Plateau de Bure Interferometer ($v = [-24, -12]$ km s^{-1}). Level contours are from $1 \text{ Jy beam}^{-1} \text{ km s}^{-1}$, in step of 0.5. Dotted contours show the negative emission ($-0.8 \text{ Jy beam}^{-1} \text{ km s}^{-1}$). The black contours outline the high velocity outflow (CO $2 \rightarrow 1$ SMA data, Beuther priv. comm. Blue-shifted emission $v = [-44, -24]$ km s^{-1} ; red-shifted emission $v = [-8, 2]$ km s^{-1} ; levels from 30 to $100 \text{ Jy beam}^{-1} \text{ km s}^{-1}$ in steps of 20). The four triangles mark the positions of the main mm dust condensations. For illustration, the direction of the highly collimated outflow (Beuther et al. 2002a) is shown by the arrows. For both flows, dashed lines are for the blue-shifted emission, solid lines for the red-shifted emission. The beam is indicated in the bottom left corner.

Table 2. Observational parameters.

Main line	Centre frequency (GHz)	Configuration	HPBW ($''$)	PA ($^\circ$)	Δv (km s^{-1})	rms (Jy/beam)
$\text{C}^{34}\text{S } 2 \rightarrow 1$	96.44	BCD	4.21×3.07	66	0.5	0.01
$\text{CH}_3\text{OH } 2_k \rightarrow 1_k v_t = 1$	96.51	BCD	4.21×3.06	66	0.5	0.01
$\text{CH}_3\text{OH } 2_k \rightarrow 1_k v_t = 1$	96.51	AB	1.85×1.36	26	1.0	0.004
$\text{CH}_3\text{OH } 2_k \rightarrow 1_k v_t = 0$	96.72	BCD	4.19×3.04	65	8	0.01
$\text{CH}_3\text{CN } 13_k \rightarrow 12_k$	238.90	BCD	2.12×1.26	77	0.8	0.03
$\text{C}^{34}\text{S } 5 \rightarrow 4$	241.08	AB	0.77×0.55	13	1.5	0.01
$\text{CH}_3\text{OH } 5_k \rightarrow 4_k v_t = 1$	241.30	AB	0.77×0.55	13	1.5	0.01
$\text{CH}_3\text{OH } 5_k \rightarrow 4_k v_t = 0$	241.85	BCD	2.58×1.35	80	0.8	0.03
$\text{H}_2\text{CS } 7_{1,6} \rightarrow 6_{1,5}$	243.98	AB	0.77×0.55	8	1.5	0.01
$\text{SO}_2 14_{0,14} \rightarrow 13_{1,13}$	244.25	AB	0.77×0.55	8	1.5	0.01
$\text{CH}_3\text{OH } 7_k \rightarrow 6_k v_t = 0, 1$	338.72	comp.-ext.	1.93×1.14	86	1.0	0.1

with a $v_{\text{lsr}} = -17.6 \text{ km s}^{-1}$. Bandpass calibration was done with Jupiter, Uranus, Callisto, and 3C 279. We used Callisto and 3C 279 for the flux calibration which is estimated to be accurate within 20%. Phase and amplitude calibration was done via frequent observations of the quasar 3C 111 about 16.3° from the phase centre. The zenith opacities, measured with the NRAO tipping radiometer located at the Caltech Submillimeter Observatory, were good during both tracks with $\tau(348 \text{ GHz}) \sim 0.18$ (scaled from the 225 GHz measurement via $\tau(348 \text{ GHz}) \sim 2.8 \times \tau(225 \text{ GHz})$). The receiver operated in a double-sided band mode with an intermediate frequency of 4–6 GHz so that the upper and lower side band were separated by 10 GHz. The correlator had a bandwidth of 2 GHz and the channel separation was 0.8125 MHz. Measured double-sided band system temperatures corrected to the top of the atmosphere

were between 150 and 500 K, mainly depending on the elevation of the source. Details on the observational setup are given in Table 2.

The initial flagging and calibration was done with the IDL superset MIR originally developed for the Owens Valley Radio Observatory and adapted for the SMA⁵. The imaging and data analysis was conducted in MIRIAD (Sault et al. 1995) and MAPPING. During the observations on November 11th, 2004, the position of the primary calibrator 3C 111 was wrong in the catalogue by $\sim 0.6''$. Therefore, we self-calibrated our secondary phase calibrator 0552+398 (16.3° from the source) shifting it in the map to the correct position. The solutions were then applied to IRAS 05358+3543.

⁵ The MIR cookbook by Charlie Qi can be found at <http://cfa-www.harvard.edu/~cqi/mircook.html>

2.3. Single-dish observations with the IRAM 30 m telescope

In addition to the high resolution data, we mapped an area of $70'' \times 180''$ in the $5_k \rightarrow 4_k v_t = 0$ CH₃OH band, with the HERA receiver (Schuster et al. 2004) at the IRAM 30 m telescope in on-the-fly mode. The observations were performed in service-mode in February 2005, under excellent weather conditions (0.6–1.1 mm precipitable water vapour). The pointing was checked on Saturn and on a nearby source (0439+360) and was found to be accurate to $\sim 6''$. Conversion from antenna temperature to main-beam brightness temperature was performed by using a beam efficiency of 0.48⁶. The beam of the 30 m telescope at 241.8 GHz is $\sim 10.2''$. Unfortunately, the overlapping in the UV plane of our PdBI and 30 m data is poor, since the PdBI baselines start only only at 20 m, and we were not able to combine the two datasets and recover the short spacing information. The IRAM 30 m data are, however, used in the following discussion to study the extended structure of the methanol emission.

3. Observational results

In this section we present the results of the line observations performed towards IRAS 05358+3543. Since the observations were aimed at observing several bands of methanol transitions, the majority of detected lines comes from this molecule. However, emission from other molecular species with transitions close in frequency space to methanol is also detected. All detected lines are listed in Tables 3 (for CH₃OH) and 4 (for the other molecular species); the dust condensations where the lines are detected are also reported in the tables.

The large structured emission is sampled by the single dish methanol data, while the interferometric datasets allow us to zoom in on the gas around the protostars. These data range in angular resolution from $4''$ to $0.6''$, corresponding to 7200 and 1100 AU, respectively. Another property of these data is that a broad range of structures are filtered out from the observations, due to the missing short-spacing flux, from $\sim 25''$ in the BCD configuration of the PdBI at 3 mm to $\sim 6''$ in its AB configuration at 1.3 mm. This means that the various datasets are differently affected by the problem, and the comparison of transitions from different configurations is not straightforward. Moreover, the UV coverage is poorly sampled also at intermediate scales, and smaller structures can be filtered out. Comparing the single dish data for the $5_k \rightarrow 4_k v_t = 0$ band of CH₃OH to the interferometric observation confirms that the PdBI data are missing fluxes. Although we cannot perform the same comparison for the rest of the dataset, negative features due to missing short spacings, heavily corrupt the other low energy line datacubes. Thus, the interpretation of the line interferometric data is potentially affected by missing flux problems.

Although our observations are among the highest spatial resolution studies of high-mass star forming regions existing today, there are obviously still limitations to what they resolve. We know from other observations that multiplicity on smaller scales happens in star forming regions of all masses (e.g., Weigelt et al. 1999; Megeath et al. 2005). The highest linear resolution of our observations (~ 1100 AU) is reached only in one dataset, while the typical resolution of the other data is poorer. Within our own data, the two sources with the smallest separation, mm1b and mm1a, are spatially resolved only in one dataset. Therefore, we cannot exclude that higher resolution would reveal more objects,

Table 3. Table of CH₃OH detected transitions. In Col. 4, ★ is used to indicate the lines with extended emission; (?) for tentative detections.

Transition	Rest frequency (GHz)	E_{upper} (K)	Detections ^a
$E 2_1 \rightarrow 1_1 v_t = 1$	96.492	298	1a
$E 2_0 \rightarrow 1_0 v_t = 1$	96.493	308	1a
$A 2_0 \rightarrow 1_0 v_t = 1$	96.514	431	1a(?)
$E 2_{-1} \rightarrow 1_{-1} v_t = 0$	96.739 ^b	13	1,2,3
$A 2_0 \rightarrow 1_0 v_t = 0$	96.741 ^b	7	1,2,3
$E 2_0 \rightarrow 1_0 v_t = 0$	96.745 ^b	20	1,2,3
$E 2_1 \rightarrow 1_1 v_t = 0$	96.756 ^b	28	1,2,3
$E 22_{-6} \rightarrow 23_{-5} v_t = 0$	241.043	776	1a(?)
$E 5_3 \rightarrow 4_3 v_t = 1$	241.167	452	1a
$A 5_{\pm 4} \rightarrow 4_{\pm 4} v_t = 1$	241.178	516	1a
$E 5_{-3} \rightarrow 4_{-3} v_t = 1$	241.180	357	1a
$E 5_{-4} \rightarrow 4_{-4} v_t = 1$	241.184	440	1a
$E 5_{-2} \rightarrow 4_{-2} v_t = 1$	241.187	399	1a
$A 5_2 \rightarrow 4_2 v_t = 1$	241.193	333	1a
$A 5_2 \rightarrow 4_2 v_t = 1$	241.196	333	1a
$A 5_{\pm 3} \rightarrow 4_{\pm 3} v_t = 1$	241.198	431	1a
$E 5_1 \rightarrow 4_1 v_t = 1$	241.204	326	1a
$E 5_0 \rightarrow 4_0 v_t = 1$	241.206	335	1a
$E 5_2 \rightarrow 4_2 v_t = 1$	241.211	435	1a
$E 5_{-1} \rightarrow 4_{-1} v_t = 1$	241.238	448	1a
$A 5_0 \rightarrow 4_0 v_t = 1$	241.268	458	1a
$A 5_1 \rightarrow 4_1 v_t = 1$	241.441	360	1a
$E 5_0 \rightarrow 4_0 v_t = 0$	241.700	48	1, 2, 3, line, ★
$E 5_{-1} \rightarrow 4_{-1} v_t = 0$	241.767	40	1, 2, 3, line, ★
$A 5_0 \rightarrow 4_0 v_t = 0$	241.791	34	1, 2, 3, line, ★
$A 5_{\pm 4} \rightarrow 4_{\pm 4} v_t = 0$	241.807	115	1, 2, line
$E 5_{-4} \rightarrow 4_{-4} v_t = 0$	241.813	123	1, 2, line
$E 5_4 \rightarrow 4_4 v_t = 0$	241.830	131	1, 2, line
$A 5_{\pm 3} \rightarrow 4_{\pm 3} v_t = 0$	241.833	85	1, 2, line
$A 5_2 \rightarrow 4_2 v_t = 0$	241.842 ^c	73	1, 2, line
$E 5_3 \rightarrow 4_3 v_t = 0$	241.844 ^c	83	1, 2, line
$E 5_{-3} \rightarrow 4_{-3} v_t = 0$	241.852	98	1, 2, line
$E 5_1 \rightarrow 4_1 v_t = 0$	241.879	56	1, 2, 3(?), line
$A 5_2 \rightarrow 4_2 v_t = 0$	241.888	73	1, 2, line
$E 5_{-2} \rightarrow 4_{-2} v_t = 0$	241.904 ^c	61	1, 2, 3, line, ★
$E 5_2 \rightarrow 4_2 v_t = 0$	241.905 ^c	57	1, 2, 3, line, ★
$A 5_1 \rightarrow 4_1 v_t = 0$	243.916	40	1, 2, line, ★
$E 7_{-2} \rightarrow 6_{-2, v=1}$	337.605	429	1a
$A 7_2 \rightarrow 6_2 v_t = 1$	337.636	363	1a
$E 7_{-1} \rightarrow 6_{-1} v_t = 1$	337.642	356	1a
$E 7_0 \rightarrow 6_0 v_t = 1$	337.644	365	1a
$E 7_{-4} \rightarrow 6_{-4} v_t = 1$	337.646	470	1a
$E 7_0 \rightarrow 6_0 v_t = 0$	338.125	78	1, 2, line, ★
$E 7_{-1} \rightarrow 6_{-1} v_t = 0$	338.345	71	1, 2, 3(?), line, ★
$E 7_6 \rightarrow 6_6 v_t = 0$	338.405	244	1
$A 7_0 \rightarrow 6_0 v_t = 0$	338.409	65	1, 2, 3(?), line, ★
$A 7_{\pm 5} \rightarrow 6_{\pm 5} v_t = 0$	338.486	203	1
$A 7_{\pm 4} \rightarrow 6_{\pm 4} v_t = 0$	338.513 ^c	145	1, 2, line
$A 7_2 \rightarrow 6_2 v_t = 0$	338.513 ^c	103	1, 2, line
$E 7_4 \rightarrow 6_4 v_t = 0$	338.530	161	1
$A 7_3 \rightarrow 6_3 v_t = 0$	338.541 ^c	115	1, 2, line
$A 7_3 \rightarrow 6_3 v_t = 0$	338.543 ^c	115	1, 2, line
$E 7_{-3} \rightarrow 6_{-3} v_t = 0$	338.560	128	1
$E 7_3 \rightarrow 6_3 v_t = 0$	338.583	118	1, 2, line
$E 7_1 \rightarrow 6_1 v_t = 0$	338.615 ^d	86	1, 2, line
$A 7_2 \rightarrow 6_2 v_t = 0$	338.640	103	1, 2, line
$E 7_2 \rightarrow 6_2 v_t = 0$	338.722 ^c	87	1, 2, line, ★
$E 7_{-2} \rightarrow 6_{-2} v_t = 0$	338.723 ^c	91	1, 2, line, ★

^a 1, 2, 3 indicate mm1, mm2, and mm3, respectively. 1 is used for data where mm1a and mm1b are not resolved; line is used for the position ($1.2''$, $0.6''$) from mm2.

^b The $2_k \rightarrow 1_k$ quartet of lines is unresolved in velocity.

^c Blend of lines.

^d Blend with the $20_{1,19} \rightarrow 19_{2,18}$ SO₂ line at 338.612 GHz.

⁶ <http://www.iram.fr/IRAMES/>

Table 4. Table of observed transitions from other molecular species. In Col. 4, ★ is used to indicate the lines with extended emission.

Transition	Rest frequency (GHz)	E_{upper} (K)	Detections ^a
C ³⁴ S 2 → 1	96.413	7	1, 2, 3, ★
C ³⁴ S 5 → 4	241.016	35	1
CH ₃ CN 13 ₆ → 12 ₆	238.972	337	1
CH ₃ CN 13 ₅ → 12 ₅	239.022	259	1
CH ₃ CN 13 ₄ → 12 ₄	239.065	195	1
CH ₃ CN 13 ₃ → 12 ₃	239.096	145	1, line
CH ₃ CN 13 ₂ → 12 ₂	239.119	109	1
CH ₃ CN 13 ₁ → 12 ₁	239.133	87	1, line
CH ₃ CN 13 ₀ → 12 ₀	239.138	80	1, line
HDO 2 _{1,1} → 2 _{1,2}	241.561	95	1
SO ₂ 5 _{2,4} → 4 _{1,3}	241.616	24	1, line
HNCO 11 _{2,10} → 10 _{2,9}	241.704	243	1
HNCO 11 _{2,9} → 10 _{2,8}	241.708	243	1
HNCO 11 _{0,11} → 10 _{0,10}	241.774	70	1
H ₂ CS 7 _{1,6} → 6 _{1,5}	244.048	60	1
SO ₂ 14 _{0,14} → 13 _{1,13}	244.254	94	1
C ³⁴ S 7 → 6	337.396	65	1, line
H ₂ CS 10 _{1,10} → 9 _{1,9}	338.083	102	1
SO ₂ 18 _{4,14} → 18 _{3,15}	338.306	197	1
SO ₂ 20 _{1,19} → 19 _{2,18}	338.612 ^b	199	1

^a 1, 2, 3 indicate mm1, mm2, and mm3, respectively. 1 is used for data where mm1a and mm1b are not resolved; line is used for the position (1.2'', 0.6'') off of mm2.

^b Blend with the 7₁ → 6₁ $v_t = 0$ CH₃OH-*E* line at 338.615 GHz.

and that the parameters we derive do not sample the gas around a single protostar. However, if this was the case, the multiple unresolved sources would form from the same reservoir of dust and gas. Assuming that they are gravitationally bound, the parameters derived in our current study would still be relevant to the analysis of the collapsing cores.

3.1. Extended emission

Emission from relatively low excitation lines is extended, as shown in Fig. 1a, where the integrated intensity of the 5₀ → 4₀, $v_t = 0$ CH₃OH-*A* transition taken with the 30 m telescope is presented.

For methanol, the emission at the cloud velocity shows a distribution very similar to the continuum emission. The offset of the line emission peak from the continuum peak is real, since it was already observed in methanol and in other molecular species (Beuther et al. 2002a). In their single-dish observations, Beuther et al. (2002a) detected red and blue non-Gaussian emission in the 5_{*k*} → 4_{*k*} methanol band, and suggested that both emissions are associated with a third outflow in the region to the west of the continuum peak. Their results are confirmed by our data, which show a bipolar distribution in the low excitation transitions of CH₃OH (Fig. 1a) with a better signal-to-noise ratio. Within the pointing uncertainties and the low resolution of the data, the centre of this outflow seems to be associated with one of the H¹³CO⁺ peaks (indicated by a pentagon in Fig. 1a) detected by Beuther et al. (2002a). If this were the case, our observations would solve the problem of the powering source of the third outflow of the region (*C* in the notation of Beuther et al. 2002a), which was previously not assigned. However, higher angular resolution is needed to assign the centre of this flow beyond a doubt.

The interpretation of the interferometric data of the same transition is not as straightforward as for the single-dish data. In

Fig. 1b, the integrated intensity of the 5₀ → 4₀ CH₃OH-*A* line is shown as seen in the PdBI observations, together with the direction of the two outflows originating from the vicinity of mm1. The region west of the dust cores, where the bipolar distribution is detected in the single-dish data, is only partially in the field of view of the PdBI observations. The intensity map is strongly affected by missing flux problems, which results in filtering out the extended emission. For this reason, the PdBI map of this transition looks clumpy. The emission is detected all over the dust continuum peaks, often red- and/or blue-shifted. These emission spots could be caused by the high velocity CO outflow originating from the vicinity of mm1 (see Fig. 1b). However, we refrain from a further discussion of these features, given the missing short spacing information of our methanol data.

The distribution of C³⁴S line is puzzling (Fig. 2). While the 2 → 1 line extends over an area of approximately 20'' × 20'' around the main dust condensations, and the 7 → 6 transition is found in association with mm1 (although marginally detected) and towards mm2, the 5 → 4 line is detected only on mm1a and mm1b (see Fig. 2). In the 5 → 4 C³⁴S line, two velocity components (see discussion on mm1 in Sect. 3.2) are detected, one at $v_{\text{lsr}} \sim -17.6 \text{ km s}^{-1}$ and the other at $v_{\text{lsr}} \sim -13 \text{ km s}^{-1}$, the first on mm1a and the second on mm1a and on the vicinity of mm1b. The emission of the 5 → 4 C³⁴S line extends to the south-west, as does that of the 7 → 6 line. However, the spectra are noisy, and the line is detected with a significance level not better than 2 σ . In Fig. 2, the level contours start from a value of 3 σ , and the feature on the south-west of mm1a is not seen in the 5 → 4 transition.

Olmí & Cesaroni (1999) studied the excitation of CS and C³⁴S towards a sample of ultra-compact HII regions, and found, as expected given the energies of the levels involved, that the 5 → 4 C³⁴S transition is usually stronger than the 7 → 6 line, making the non detection of the 5 → 4 line on mm2 difficult to interpret. However, this line was observed in the AB configurations of the PdBI interferometer, where source structures larger than 6'' are filtered out. Therefore, the unexpected spatial distribution of this transition, as well as its profile, can be an artifact due to the missing short spacing information.

Comparing the spatial distribution of the 2 → 1 and 7 → 6 C³⁴S lines, which are affected by missing flux problems on larger scales ($\geq 30''$ and $\geq 16''$, respectively), it emerges that they do not peak on the protostellar cores, but in the gas between the cores, where the temperature most likely drops down. Observations of the hot core in G29.96-0.02 (Beuther et al. 2007b), with the same frequency setup of our SMA data, show a similar effect, with the 7 → 6 C³⁴S line peaked in the gas between the (sub)mm continuum peaks. On the other hand, in G29.96-0.02, the 8₈ → 7₇ ³⁴SO line peaks on the hot core. Since CS should desorb from dust grains relatively early in the evolution of the source (Viti et al. 2004), while the SO and SO₂ abundances should increase with time, Beuther et al. (2007b) interpret the distributions of C³⁴S and ³⁴SO in G29.96-0.02 as an evolutionary indicator. In our case, we did not detect the 8₈ → 7₇ ³⁴SO transition toward IRAS 0535+3543. However, we observed four transitions of SO₂, and all peak on the main dust condensation mm1 (Fig. 3). Although the evolutionary scenario outlined for G29.96-0.02 seems to be confirmed by our observations of the 2 → 1 and 7 → 6 C³⁴S, and of the SO₂ transitions, the distribution of the 5 → 4 C³⁴S line does not find an easy interpretation within this theory.

Similarly to C³⁴S, also H₂CS shows different morphologies in the two transitions in our datasets (Fig. 3), with the 10_{1,10} → 9_{1,9} line ($E_{\text{up}} \sim 100 \text{ K}$) having a second peak at an

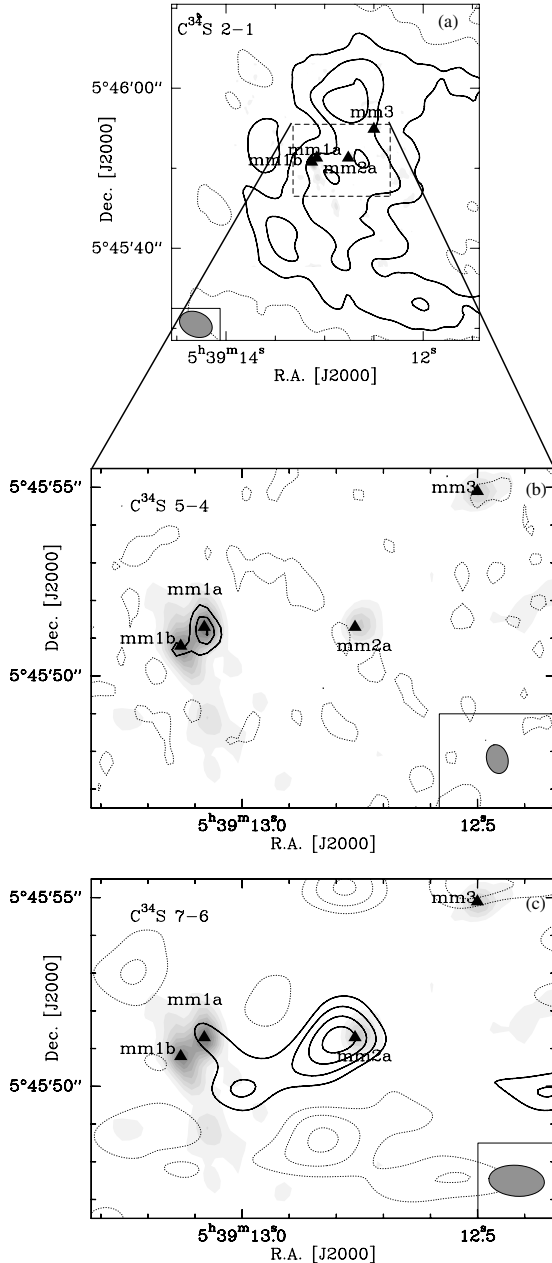


Fig. 2. In grey scale the 1.3 mm continuum emission (from the AB configuration of the Plateau de Bure Interferometer). The black contours show the integrated line intensity of the $2 \rightarrow 1$ a), the $5 \rightarrow 4$ b), and of the $7 \rightarrow 6$ $C^{34}S$ lines c). Level contours are from $0.1 \text{ Jy beam}^{-1} \text{ km s}^{-1}$ in steps of 0.2 for the $2 \rightarrow 1$ transition; from $0.3 \text{ Jy beam}^{-1} \text{ km s}^{-1}$ in steps of 0.3 for the $5 \rightarrow 4$ line, and from 1.5 in steps of 0.5 for the $7 \rightarrow 6$. Level contours for the continuum are in step of 0.003 from $0.003 \text{ Jy beam}^{-1}$. The dotted contours show the negative emission ($-0.1 \text{ Jy beam}^{-1} \text{ km s}^{-1}$ for the $2 \rightarrow 1$ and $5 \rightarrow 4$ lines; from -1.5 in step of $0.5 \text{ Jy beam}^{-1} \text{ km s}^{-1}$ for the $7 \rightarrow 6$ transition). The dashed lines in panel a) outline the region shown in the other two panels. The different beams are also given.

offset position from mm2 (see the discussion below), while the $7_{1,6} \rightarrow 6_{1,5}$ is found only on mm1a, despite its lower level energy ($E_{\text{up}} \sim 60 \text{ K}$). We believe that these data are heavily contaminated by missing flux problems at intermediate and short scales, and refrain from any analysis of this molecular species.

3.2. Molecular emission from the dust cores

The molecular spectra of the three main dust condensations, mm1, mm2 and mm3, differ significantly from each other, reflecting the different physical conditions, and probably time evolution, of the dust cores. Maps of the integrated intensity of several transitions are shown in Figs. 3 and 4. All high excitation lines peak on mm1, and specifically on mm1a for the dataset where the cores mm1a and mm1b are spatially resolved. However, several moderately excited ($E_{\text{up}} \leq 130 \text{ K}$) methanol lines are extended towards the second dust core mm2, and show a peak of intensity at $(1.2'', 0.6'')$ from mm2.

Source mm1: Fig. 5 presents the observed spectral bands at 238, 241 and 338 GHz, respectively, towards the main dust condensation mm1. High excitation ($E_{\text{up}} > 200 \text{ K}$) transitions are detected towards this core; however, the datasets where the two dust condensations mm1a and mm1b are resolved, show that the emission from high excited lines is associated only with mm1a. Only the $5 \rightarrow 4$ $C^{34}S$ transition ($v \sim -13.4 \text{ km s}^{-1}$) is detected on mm1b. The lack of molecular emission from mm1b could be a bias of the observations: the two dust condensations are resolved only in the AB configuration of the PdBI, which was aimed at the detection of torsionally excited lines of methanol and had the $5 \rightarrow 4$ $C^{34}S$ as the only low excitation transition. The two condensations have very similar properties for the continuum emission (Beuther et al. 2007a). However, other observations suggest that mm1a and mm1b are indeed of different nature, as methanol class II masers (Minier et al. 2000), and a mid-infrared source (Longmore et al. 2006) are detected on mm1a, but not on mm1b. A similar chemical differentiation of two cores of very close masses was recently found by Zhang et al. (2007) in the high-mass (proto)stellar cluster AFGL5142. As suggested for AFGL5142, a possible interpretation of our observations is that mm1b is in an earlier evolutionary phase than mm1a, still not characterised by a rich chemistry.

Source mm1a: several methanol transitions, in the ground state as well as in the first torsionally excited level, show two velocity components. The same profile is found in the $12_k \rightarrow 11_k$ CH_3CN band (SMA data, Beuther priv. comm.) and in the $13_k \rightarrow 12_k$ lines, in the $7_{1,6} \rightarrow 6_{1,5}$ H_2CS line, and in the $5 \rightarrow 4$ $C^{34}S$ transition. HNC is also showing the same behaviour in the $11_{0,11} \rightarrow 10_{0,10}$ line at ~ -17.8 and $\sim -15.3 \text{ km s}^{-1}$. Two peaks are also detected in the $11_{2,9} \rightarrow 10_{2,8}$ transition, but the blend with the $5_0 \rightarrow 4_0$ CH_3OH-E line and with the $11_{2,10} \rightarrow 10_{2,9}$ transition complicates the interpretation of this profile. On the other hand, the SO_2 and HDO lines at $\sim 241.6 \text{ GHz}$ show only one velocity component, peaked at -16.6 and -14.9 km s^{-1} , respectively. For the HDO line, this corresponds to the velocity in between the two peaks detected in the other transitions. An example of the double peak profile of mm1a is given in Fig. 6, where part of the $5_k \rightarrow 4_k, v_t = 1$ CH_3OH band is shown. For the $7_{1,6} \rightarrow 6_{1,5}$ H_2CS and the $5 \rightarrow 4$ $C^{34}S$ lines, this profile could be caused by missing flux; self absorption or missing flux problems could affect the low energy transitions of methanol. The hypothesis of self absorption is strengthened by the profile of HDO transition. However, since the double-peaked profile is found also at high energies, where the optical depth is unlikely to be high, even in rare molecular species, we believe that the two peaks are, at least for the torsionally excited lines of CH_3OH , for CH_3CN and HNC, real, and not due to self absorption. In several cases, overlap between different lines complicates the identification of the two components; however, a few lines ($5_0 \rightarrow 4_0$ and $5_{-1} \rightarrow 4_{-1}$ $v_t = 1$ CH_3OH ; $13_4 \rightarrow 12_4$ CH_3CN) do not overlap with any other transitions. By Gauss fitting their line profiles,

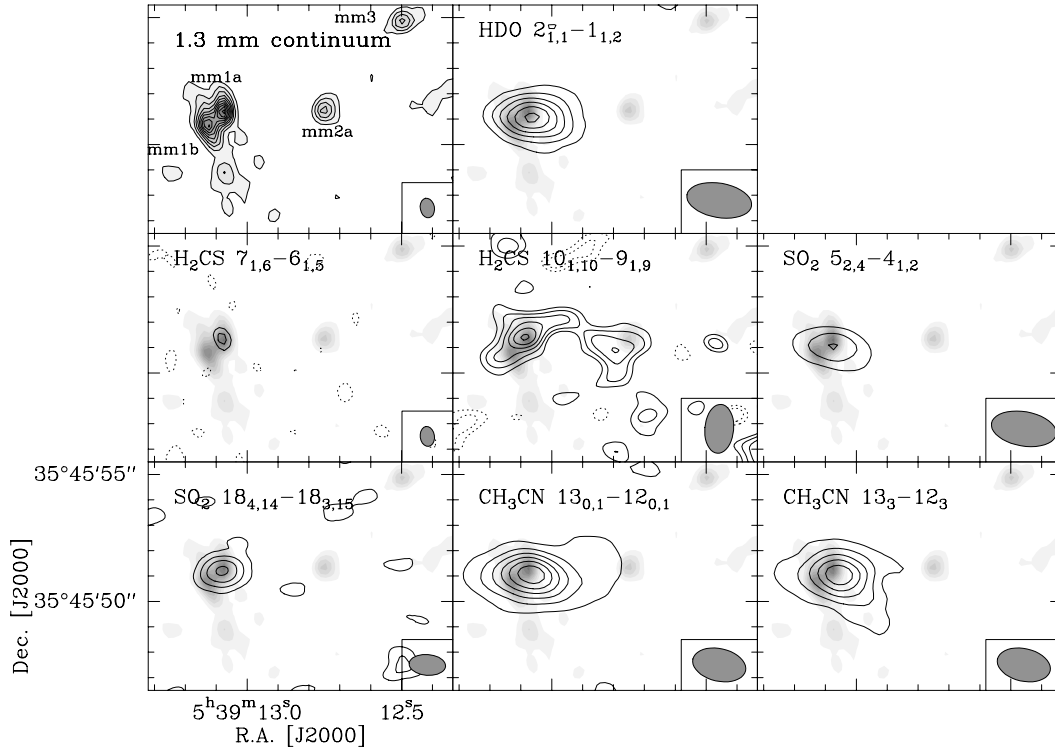


Fig. 3. Compilation of integrated intensity maps of transitions from several molecular species, shown as black contours. In grey scale (and in the solid contours in the first panel) the 1.3 mm continuum emission from the AB configuration of the Plateau de Bure Interferometer. Level contours for the line images are from $0.5 \text{ Jy beam}^{-1} \text{ km s}^{-1}$, in step of 0.3; for the $7_{1,6} \rightarrow 6_{1,5}$ H_2CS transition, from $0.3 \text{ Jy beam}^{-1} \text{ km s}^{-1}$, and from $1 \text{ Jy beam}^{-1} \text{ km s}^{-1}$ for the $18_{4,14} \rightarrow 18_{3,15}$ SO_2 line. Level contours for the $13_{0,1} \rightarrow 12_{0,1}$ CH_3CN transitions are in step of $0.6 \text{ Jy beam}^{-1} \text{ km s}^{-1}$. The dotted contours show the negative emission: for the $7_{1,6} \rightarrow 6_{1,5}$ H_2CS transition $-0.1 \text{ Jy beam}^{-1} \text{ km s}^{-1}$; for the $10_{1,10} \rightarrow 9_{1,9}$ H_2CS line -1.5 and $-1.2 \text{ Jy beam}^{-1} \text{ km s}^{-1}$. Continuum contours are the same as in Fig. 2. The beam is shown in the right bottom corner.

we derive linewidths of ~ 3 and $\sim 4 \text{ km s}^{-1}$, and system velocities of $\sim -17.6 \text{ km s}^{-1}$ and $\sim -11.6 \text{ km s}^{-1}$, respectively. Both velocity components peak on mm1a.

We fitted the peak position of each velocity channels of the $5_{-1} \rightarrow 4_{-1} v_t = 1$ $\text{CH}_3\text{OH-}E$ line, and detected a velocity gradient along an elongated structure (Fig. 7a). This linear structure seems to be shifted from the millimetre continuum peak. The same velocity gradient of the $v_t = 1$ methanol lines is found in the $19 \rightarrow 18$ OCS line at 231 GHz (detected with the SMA, Beuther priv. comm.), and in the 6.7 GHz methanol maser transition (Minier et al. 2000). In Fig. 7a, we show for comparison the positions of the velocity channels of the maser line, and in Fig. 7b the first moment map of the $19 \rightarrow 18$ OCS transition. Moreover, observations with the SMA with an angular resolution of $\sim 3''$ (Beuther, priv. comm) show that the $2 \rightarrow 1$ C^{18}O line is associated with the high velocity outflow of Beuther et al. (2002a), and has a velocity gradient perpendicular to the linear structure detected in methanol. While an unresolved expanding or contracting shell of gas would also produce the double-peaked profile detected towards mm1a, the linear velocity gradient detected in methanol and OCS cannot be explained by these scenarios.

The line profile detected towards mm1a is reminiscent of the double-peaked profiles found in low and intermediate mass tilted circumstellar disks, in optically thin and thick lines (Beckwith & Sargent 1993). Moreover, the double-peaked profile arises from a region ($R \leq 550 \text{ AU}$) comparable in size to the candidate disks surrounding high-mass (proto)stars (for a compilation of them, see Cesaroni et al. 2007). The detection of a velocity gradient is

not conclusive of a circumstellar disk. However, we believe that the velocity structure detected in methanol and perpendicular to the high-velocity outflow, together with the double-peaked profile, and the size of the emitting gas are strongly suggestive of a rotating structure in IRAS 05358-mm1a. To investigate whether this structure is a circumstellar disk or a toroid like the ones discussed by Cesaroni et al. (2007), higher linear and velocity resolutions are needed to study the velocity field of the innermost gas around mm1a. We note, however, that toroids have typical radii of several thousands AU, while the radius of the structure around mm1a has an upper limit of 550 AU.

Alternatively, two different hot components with a separation of less than 1100 AU would also produce a double-peaked profile, and a velocity gradient along a linear structure. Since the two lines have very similar intensities and linewidths, the physical conditions in the two cores would be comparable (as derived in paragraph Sect. 4.1). The total mass of the binaries can be derived via (e.g., Chen et al. 2006)

$$M_{\text{tot}} = \frac{A \times \Delta v^2}{G \times \sin^2(i)} \quad (1)$$

where A is the semi-major axis of the elliptical orbit of the two stars, G the gravitational constant, i the inclination angle, which is unknown, and Δv the relative velocity between the two cores. An upper limit to the major axis is given by the resolution of the data ($0.6''$, corresponding to $\sim 1100 \text{ AU}$, at this distance). In Sect. 4.1, the sizes of the two sources are derived by fitting the $13_k \rightarrow 12_k$ CH_3CN band. Therefore, the lower limit to the major axis of the orbit is taken as the sum of their radii, corresponding

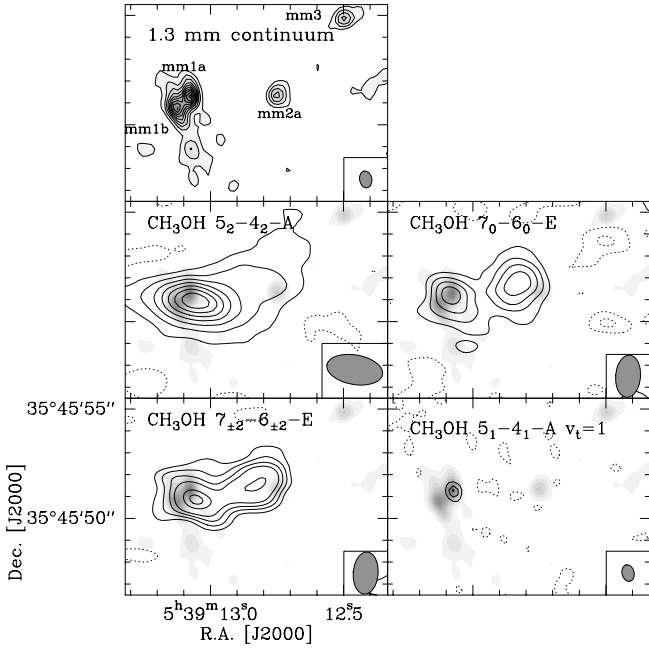


Fig. 4. Compilation of integrated intensity maps of CH₃OH, shown as black contours. In grey scale (and in the solid contours in the first panel) the 1.3 mm continuum emission from the AB configuration of the Plateau de Bure Interferometer. Level contours for the line images are from: 0.3 Jy beam⁻¹ km s⁻¹ in step of 0.4, 1 Jy beam⁻¹ km s⁻¹ in step of 1, 1.5 Jy beam⁻¹ km s⁻¹ in step of 1, 0.2 Jy beam⁻¹ km s⁻¹ in step of 0.2, respectively. Dotted contours are used for negative values: for the 5₂ → 4₂-A line -0.2 Jy beam⁻¹ km s⁻¹; -2 and -1 Jy beam⁻¹ km s⁻¹ for the 7₀ → 6₀-E line; -2 Jy beam⁻¹ km s⁻¹ for the 7_{±2} → 6_{±2}-E line; -0.1 for the 5₁ → 4₁ CH₃OH-E v_t = 1 transition. Continuum contours are the same as in Fig. 2. The beam is shown in the right bottom corner.

to 0.2'' (360 AU), which is in agreement with the extension of the linear structure in Fig. 7a. Hence, the total mass of the system ranges between 22 and 7 M_⊙/sin² i, in good agreement with the value of 13 M_⊙ derived from the Lyman continuum flux (Beuther et al. 2007a).

In both cases, a rotating structure or two close-by hot cores, the single-peaked line profile of HDO would suggest that the emission is coming from a larger envelope of gas.

To discriminate between the different possibilities discussed above, higher spatial resolution observations will be required to resolve and image the system in more details. Among the current cm-mm interferometers, only the VLA in its A configuration would allow observations with a spatial resolution significantly higher than the one of our current data. Otherwise, studies of such systems at resolutions of 0.1'' or less in spectral lines other than NH₃ will be possible in the submm windows only when the Atacama Large Millimeter Array (ALMA) will come on line in the next few years.

Source mm2: the molecular spectrum of mm2 shows emission from several species, with moderately excited ($E_{\text{up}} \leq 130$ K) methanol lines. Linewidths are comparable to the one of the components in mm1, and emission is at $v = -15.3$ km s⁻¹. However, stronger emission is detected in several methanol lines at (1.2'', 0.6'') off of mm2 ($\alpha_{2000} = 05^{\text{h}}39^{\text{m}}12^{\text{s}}.86$, $\delta_{2000} = +35^{\circ}45'51''.9$), at a position where no continuum emission is detected (see Fig. 4). At the same position, the CH₃CN $k = 0, 1, 3$ lines are also detected, while the 7 → 6 C³⁴S and 10_{1,10} → 9_{1,9} H₂CS transitions have a secondary emission peak

in the vicinity of this position. Linewidths are of the order of 3.7 km s⁻¹, at the same velocity of mm2.

To rule out the hypothesis that the different distribution of the gas with respect to the dust is not real, but due to optical depth effects, the intensity of the lines should be mapped in the wings, where the optical depth is lower. Unfortunately, the signal to noise in the CH₃CN spectrum and in the SMA data, which are the two datasets less affected by line-overlapping problems, is not good enough to perform this check. However, given the range of energies of the lines showing a second peak between mm1 and mm2 (see Figs. 3 and 4), we believe that this spatial distribution is real. In Fig. 8, the CH₃CN and CH₃OH spectra are shown towards the offset position. In the rest of the paper, we will refer to this position as to mm2-line. The molecular spectrum of mm2 looks very similar to the one of mm2-line, but line intensities are usually a factor of 1.2 weaker than on mm2-line. Since the two positions have a separation of roughly half the beam size of our observations, we cannot rule out that part of the emission at mm2 is coming from mm2-line.

A possible interpretation for the molecular emission at mm2-line is that it is caused by sputtering or thermal evaporation of the grain mantles, followed by gas-phase reactions, due to the interaction with one or more of the outflows in the region (see Fig. 9). Although mm2-line is characterised by narrow features ($\Delta v_{\text{LSR}} \sim 3.2$ km s⁻¹), the emission is red-shifted respect to mm1, thus strengthening the outflow scenario. However, the detection of a high-density tracing molecule like CN₃CN at this position does not easily fit with this hypothesis. Alternatively, a low-mass dense core could be responsible for this emission. In this case, an upper limit to the mass of mm2-line can be computed from the continuum emission at 1.3 mm, assuming a temperature of 60 K as derived from the analysis of its methanol spectrum (see Sect. 4.3). This results in a mass of $M_{\text{H}_2} \sim 0.08 M_{\odot}$. In Sect. 4.3, we derive a lower limit of 10⁻⁷ for the abundance of methanol at mm2-line, which is comparable to the values found in low-mass star hot cores (Maret et al. 2005). These cores are however usually warmer than 60 K. Otherwise, the enhancement of the CH₃OH abundance can also be explained within the hypothesis that the emission is caused by the interaction of molecular outflows with the ambient molecular cloud.

Source mm3: the core mm3 presents the simplest molecular spectrum among the several dust condensations in the region. The emission associated with mm3 is extended and not coming from a compact core, as all the lines detected are seen as negative features, an artifact due to missing spacings. Therefore, only a qualitative analysis of these data is possible. Beuther et al. (2007a) computed its spectral energy distribution and derived an upper limit to the dust temperature of ~20 K, a value that is constrained by the weakness of the continuum emission at 690 GHz. In paragraph Sect. 4.3, we discuss the molecular spectrum at this position, and conclude that the gas around mm3 is cold (<30–40 K), and dense (10⁵–10⁶ cm⁻³). Therefore, our results agree with the conclusion of Beuther et al. (2007a) that mm3 is a candidate of a cold massive core in an early evolutionary stage. Our observations of CH₃OH and C³⁴S suggest that these molecules have an extended, flat distribution, and show no trace of the structure seen in the dust continuum emission, a result reminiscent of observations of low-mass starless cores (e.g., Caselli et al. 1999). Even H¹³CO⁺, a good tracer of quiescent gas, shows no peak on mm3 (Beuther et al. 2002a). These results suggest that mm3 is indeed a candidate massive starless core. However, high angular resolution observations that trace the dense gas and investigate potential signs of star formation activity are needed to test this hypothesis.

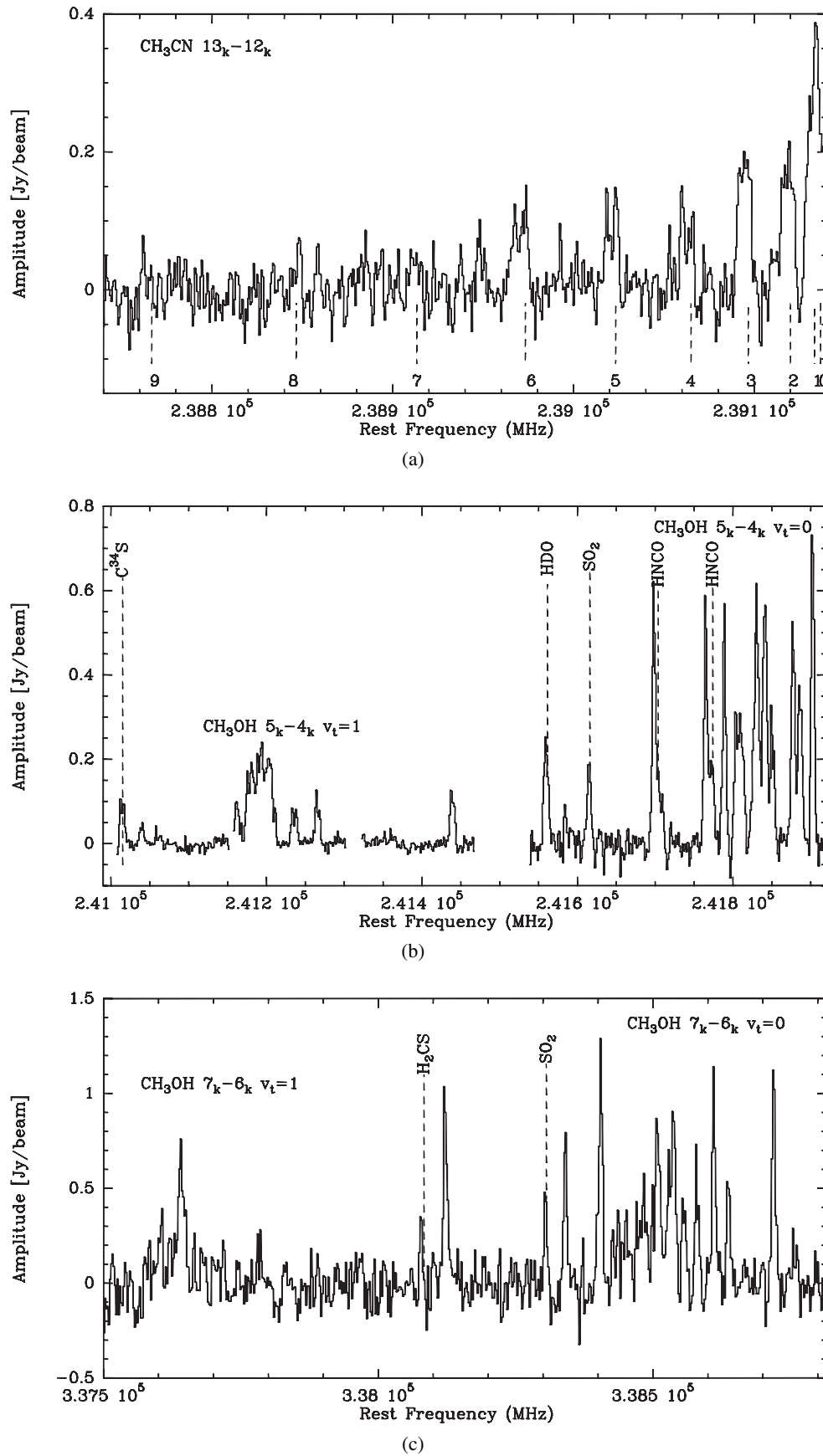


Fig. 5. Molecular spectrum of mm1. The two cores, mm1a and mm1b, are resolved only for $5_k \rightarrow 4_k v_t = 1$ CH_3OH lines at ~ 241.2 GHz in Fig. 5b. For CH_3CN , different K numbers are marked with dashed lines in the lower part of the spectrum (Fig. 5a). The features from other molecular species are labelled with the name of the molecule. Not labelled transitions are methanol lines.

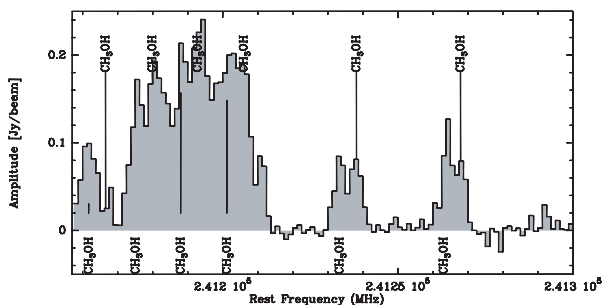


Fig. 6. Spectrum of mm1a at 241.2 GHz. The upper labels indicate the rest frequencies of the CH_3OH lines for a velocity of -17.6 km s^{-1} , while the lower labels show the same transitions for a velocity of -11.6 km s^{-1} .

4. Derivation of physical parameters

4.1. CH_3CN

The physical properties of the gas around mm1 are derived by the analysis of the $13_k \rightarrow 12_k$ CH_3CN lines. The analysis was carried out with the Xclass program (discussed in Comito et al. 2005), which uses an LTE model to produce synthetic spectra, and compares them to the observations. The molecular data are from the CDMS (Müller et al. 2001) and JPL (Pickett et al. 1998) databases. The parameters defining the synthetic spectrum are: source size, rotation temperature, column density, velocity width and velocity offset (with respect to the systemic velocity of the object). Several velocity components, which are supposed to be non-interacting (i.e. the intensities add up linearly), can be used.

Given the low signal-to-noise ratio of the spectra, it is possible to perform this analysis only on mm1. For this position, we assumed that all the CH_3CN transitions trace the same warm, dense gas around the central object and come from the two velocity components detected in several molecular species (see paragraph Sect. 3.2), although the lower excitation lines may have contribution from a more extended component (Fig. 3). Since the line profiles consist of two peaks of the same intensity, we used the same physical conditions for the two components. The source size is degenerate with temperature in the case of completely optically thick lines, and with column density for completely optically thin lines. In our case, the $k > 3$ lines are optically thin, while the $k \leq 3$ are optically thick. Therefore, the degeneracy between source size and column density can be solved. Constrains on the column density of CH_3CN come also from the non detection of the $13_k \rightarrow 12_k$ $\text{CH}_3^{13}\text{CN}$ band, which is very close in frequency to the CH_3CN lines. We found that the source size is constrained to $\sim 0.2''$ for each component, in agreement with the size of $0.2\text{--}0.3''$ of the linear structure of Fig. 7a. For this value, the best fit corresponds to a temperature of 220 K, and a column density of $\sim 4 \times 10^{16} \text{ cm}^{-2}$ per velocity component. The uncertainties on these values are reported in Table 5. Assuming that the CH_3CN emission comes from mm1a, and using the hydrogen column density derived by Beuther et al. (2007a) for the AB configuration data at 1.2 mm ($N_{\text{H}_2} \sim 2.2 \times 10^{24} \text{ cm}^{-2}$), this results in a total abundance of CH_3CN relative to H_2 of 4×10^{-8} , which is typical of hot cores (e.g., Hatchell et al. 1998). However, Beuther et al. (2007a) derived the H_2 column density for a temperature of 50 K, while our estimate of T_K is higher. The abundance increases to 2×10^{-7} , when re-computing the H_2 column density of mm1a at 220 K ($N_{\text{H}_2} \sim 4.6 \times 10^{23} \text{ cm}^{-2}$).

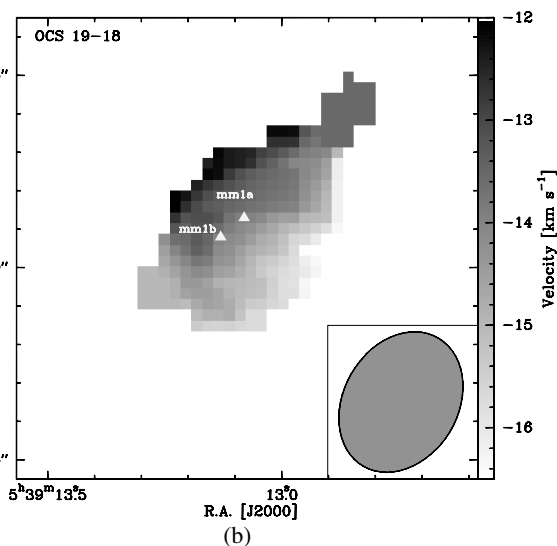
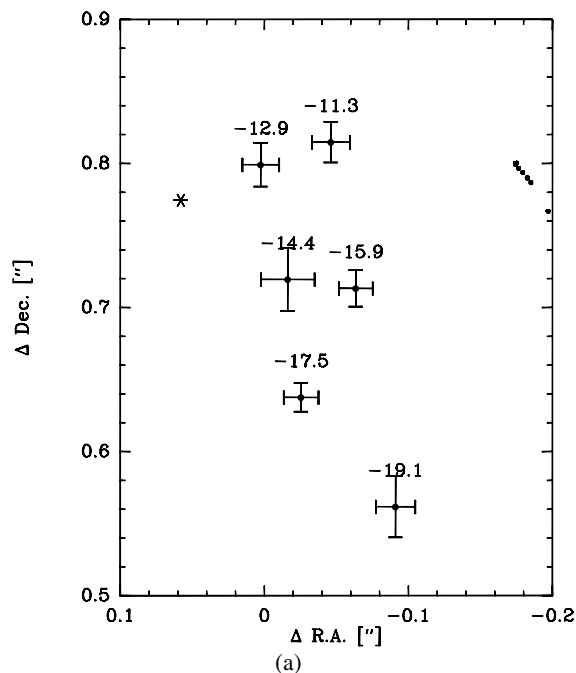


Fig. 7. a) Presented is the position-position (P-P) diagram of the $5_{-1} \rightarrow 4_{-1} v_t = 1-E$ CH_3OH line. The star marks the position of the 1.3 mm continuum peak. The values above each mark are the LSR velocities of the corresponding channels. The error bars represent statistical errors of the fits. The error on the position of the continuum peak are negligible. The black dots on the east mark the positions of the velocity channels of the 6.7 GHz methanol maser (Minier et al. 2000). The offset between the two linear structures can be accounted for pointing uncertainties, and error in the absolute position of the VLBI data. **b)** First moment map of the $19 \rightarrow 18$ OCS transition. The white triangles mark the positions of the dust condensations mm1a and mm1b. The beam is shown in the bottom right corner.

4.2. SO_2

Four SO_2 transitions were detected towards the main condensation mm1. They range in energy of the upper level from ~ 24 to 200 K; therefore, although they look point-like in all observations, they likely trace different gas around mm1. We analysed the SO_2 emission by means of the LTE technique discussed in paragraph Sect. 4.1. Since the lines do not show any

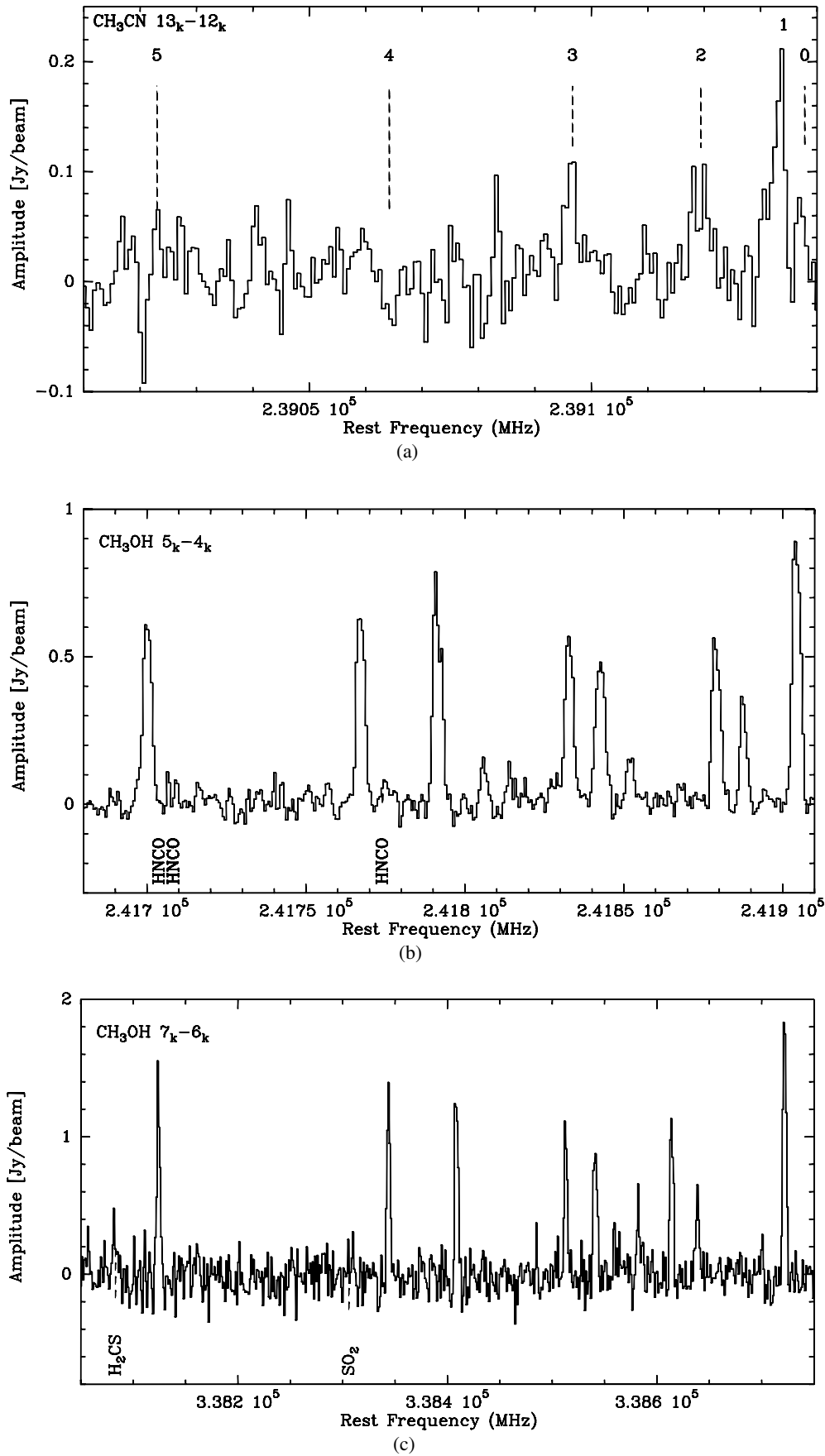


Fig. 8. Molecular spectra towards mm2-line [$\alpha_{2000} = 05^{\text{h}}39^{\text{m}}12^{\text{s}}.86$, $\delta_{2000} = +35^{\circ}45'51''.9$]. For CH₃CN, different K numbers are marked with dashed lines in the upper part of the spectrum (Fig. 8a), while only the species are given for the other molecules. Not labelled transitions are methanol lines.

Table 5. Overview of the physical parameters in IRAS 05358+3543: – indicates parameters which cannot be derived with our data.

Core	Θ [$''$]	T [K]	n [cm^{-3}]	N [cm^{-2}]	X	$N_{\text{H}_2}^a$ [cm^{-2}]
CH₃OH						
mm1a ^b	0.15	220 (75–270)	–	4×10^{18} (4×10^{17} – 1×10^{19})	10^{-5}	4.6×10^{23}
mm2	2.5	60 (40–80)	$>6 \times 10^6$	4×10^{15} (4×10^{15} – 5×10^{15})	6×10^{-9}	2.7×10^{23}
mm2-line	2.5	60 (40–110)	$>6 \times 10^6$	7×10^{15} (1×10^{15} – 2×10^{16})	10^{-7}	5×10^{22}
mm3	–	<40	10^5 – 10^6	–	–	4.9×10^{24}
CH₃CN						
mm1a ^b	0.2	220 (120–330)	–	8×10^{16} (4×10^{16} – 4×10^{18})	2×10^{-7}	4.6×10^{23}
SO₂						
mm1	1.0	150 (>60)	–	1×10^{16} (5×10^{15} – 5×10^{16})	5×10^{-8}	2×10^{23}

^a Derived from the 1.3 mm continuum data presented by Beuther et al. (2007a) and using the temperature derived from each molecular species.

^b The values refer to the total column density of the two velocity components.

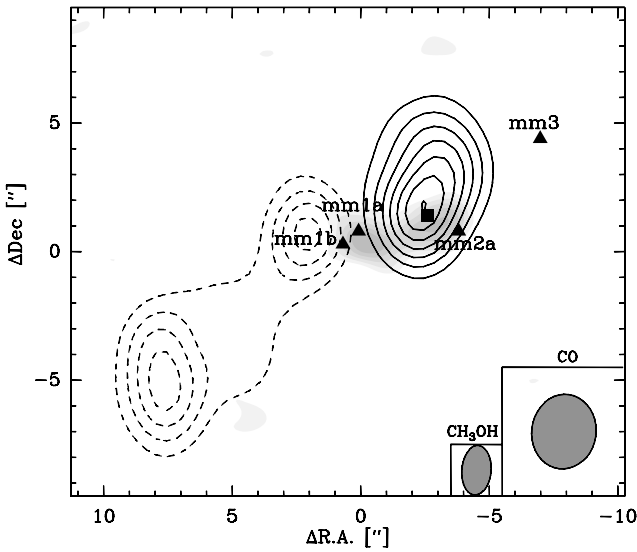


Fig. 9. In grey scale, the integrated intensity of the $7_2 \rightarrow 6_2 v_t = 0$ CH₃OH-*E* with the SMA (from $2.5 \text{ Jy beam}^{-1} \text{ km s}^{-1}$ in step of 1), overlaid on the CO $2 \rightarrow 1$ high velocity outflow (SMA, Beuther, priv. comm. Blue: solid lines $v = [-44, -24] \text{ km s}^{-1}$; red: dashed lines $v = [-8, 2] \text{ km s}^{-1}$; levels from $1.5 \text{ Jy beam}^{-1} \text{ km s}^{-1}$ in steps of 1). The four triangles mark the positions of the main mm dust condensations; the square outlines the mm2-line position.

trace of the double-peaked profile detected in other molecular species, we used a model with one velocity component for SO₂. Assuming a source size of $1''$, the best fit is found for $T = 150 \text{ K}$ and $N(\text{SO}_2) = 10^{16} \text{ cm}^{-2}$, which corresponds to an abundance of SO₂ relative to molecular hydrogen of 2×10^{-8} using $T_{\text{dust}} = 50 \text{ K}$ ($N_{\text{H}_2} \sim 6.6 \times 10^{23} \text{ cm}^{-2}$), and of $\sim 5 \times 10^{-8}$ for a temperature of 150 K ($N_{\text{H}_2} \sim 2 \times 10^{23} \text{ cm}^{-2}$). The errors on the parameters are listed in Table 5.

4.3. CH₃OH

For the analysis of the CH₃OH spectrum, we used a technique similar to the one discussed for CH₃CN (Sect. 4.1) and implemented to the LVG approximation (Leurini et al. 2004, 2007). Since methanol is detected at several positions, in the following discussion the properties of each dust condensation will be discussed separately. The errors on the parameters are listed in Table 5 for each condensation.

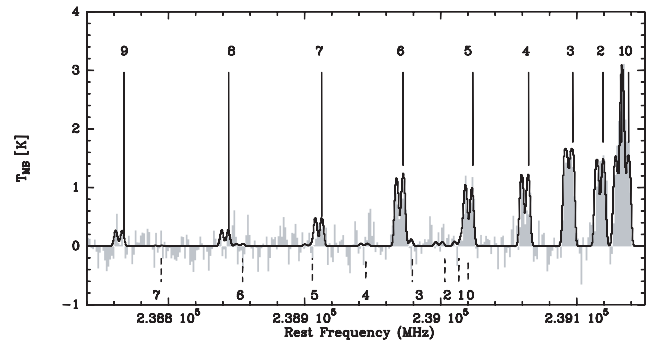


Fig. 10. Spectrum of the $13_k \rightarrow 12_k$ CH₃CN band towards the main dust condensation mm1; overlaid on the data, in black, the best fit synthetic spectrum. All CH₃CN lines are labelled in the upper axis for the velocity component $v = -17.6 \text{ km s}^{-1}$. The frequencies of the corresponding CH₃CN transitions are labelled in the lower axis.

Source mm1a: in our analysis of mm1a, we included only emission coming from the $v_t = 1$ lines, as their optical depth is lower than for the ground state, and their emission is confined to the gas around the dust condensation, while the $v_t = 0$ transitions are more extended, and are affected by problems of missing flux. Moreover, the $v_t = 1$ lines have similar level energies, while the ground state transitions in our data range from a few K to $\sim 200 \text{ K}$, thus not tracing the same gas. The model includes the three torsionally excited bands observed, the $2_k \rightarrow 1_k$ at 3 mm, the $5_k \rightarrow 4_k$ at 3 mm, and the $7_k \rightarrow 6_k$ at 0.8 mm. Infrared pumping by thermal heating of the dust is included in the form of an external grey-body (Leurini et al. 2007), with $\beta = 1.6$ and $\tau_{100 \mu\text{m}} = 1.5$. This is necessary to explain the excitation of the torsionally excited lines, as, with very high critical densities (10^{10} – 10^{11} cm^{-3}) and high level energies ($T \geq 200 \text{ K}$), they can be hardly populated by collisions, but trace the IR field instead. On the other hand, the ground state lines can be populated by collisions and by the infrared pumping. Leurini et al. (2007) investigated the effects of infrared pumping on the excitation of methanol, and found that, as in the case of other molecules (e.g. CS, Carroll & Goldsmith 1981), the infrared pumping mimics the excitation by collisions of the $v_t = 0$ lines. This results in a degeneracy between the density and the infrared field of the thermal dust which makes any determination of the density through the analysis of the ground state lines of methanol impossible, for sources like hot cores. As in the discussion in paragraph Sect. 4.1, we used two velocity components to model the data.

The best fit is reached for values very similar to the ones derived with CH₃CN, source sizes of $0.15''$ and a temperature of

220 K. As the line intensities are very similar in the two velocity components in almost all lines, the same parameters are derived for both of them. The column density for methanol is equal to $\sim 2 \times 10^{18} \text{ cm}^{-2}$ per component, which, using the H_2 column density derived by Beuther et al. (2007a) for mm1a for 50 K, corresponds to a total abundance of methanol relative to molecular hydrogen of 2×10^{-6} , or to 10^{-5} if we adopt 220 K as dust temperature. Both values are typical of massive hot cores (Menten et al. 1986, 1988).

The fit well reproduces the intensities of the $J = 5, 7$ series, but it fails to correctly predict the strength of the lines at 96 GHz, which are weaker in the model than in the observations. A plausible explanation is that 3 mm lines come from a more extended region than the others, and therefore the real beam dilution is less than that obtained in the model with a source size of $0.15''$. With the resolution of our data, we cannot verify this hypothesis. The $2_k \rightarrow 1_k$ lines were observed in both the BCD and the AB configurations of the array, and no flux is lost in the data with the higher resolution. However, the CLEAN beam of the AB data at 3 mm is significantly larger than the one at 1.3 mm, and different emission sizes between the 3 mm and the 1.3 mm lines cannot be ruled out. Moreover, the 96 GHz lines peak at 300 K in energy of the upper level, while the other bands are at higher energies (330–530 K), and they are therefore more likely to trace the gas closer to the central heating source.

Source mm2: since no torsionally excited lines are detected toward mm2, the analysis on the methanol spectrum was performed on the ground state lines, and no external radiation field was used in the calculations. As discussed for mm1a, the analysis of these lines is not trivial, as they range in energy of the upper level from 35 K to more than 100 K (see Table 3), and therefore trace different regions of gas. Moreover, some $v_t = 0$ lines have extended emission and are, thus, affected by missing fluxes problems. The analysis of the datacubes at 241.7 and 338 GHz shows that several methanol lines have a spatial distribution similar to that of the $5_0 \rightarrow 4_0 v_t = 0$ $\text{CH}_3\text{OH-A}$ transition (Fig. 1b). We excluded these lines from our study of mm2, and limited the analysis to the transitions that are peaked on the main dust cores. An asterisk in Table 3 marks the lines with extended emission, excluded from the analysis of mm2.

The continuum data (Beuther et al. 2007a) reveal a complex area around mm2, with several sub-sources which may not be of protostellar nature, but which could be caused by the outflows in the region. Given the relatively low resolution of the observations of the methanol ground state lines, the molecular emission detected toward mm2 could arise not only from the gas associated with the dust core mm2a, but also from the other sub-sources around it. Therefore, in modelling the molecular spectrum of mm2, we used the beam size as source size, and derived the average physical parameters of the gas over the beam. This approach is justified by the low optical depth of the methanol lines for the physical conditions found in the analysis. The same technique was used to model the methanol emission at the position ($\alpha_{2000} = 05^{\text{h}}39^{\text{m}}12^{\text{s}}.86$, $\delta_{2000} = +35^{\circ}45'51''.9$), northwest of mm2. Since no continuum emission is detected there, the nature of the molecular emission is unknown. The spectra toward the two positions, mm2 and mm2-line, are very similar: emission comes from the same transitions, which have similar linewidths, and emit at similar velocities. However, the emission from mm2-line is stronger than on mm2 in all methanol lines, hence suggesting that the methanol abundance is enhanced at this position. The best fit is found for a temperature of 60 K, and a column density of $4 \times 10^5 \text{ cm}^{-2}$ and $7 \times 10^5 \text{ cm}^{-2}$ for mm2 and mm2-line, respectively. The column densities at the

two positions are $4 \times 10^{15} \text{ cm}^{-2}$ for mm2, and $7 \times 10^{15} \text{ cm}^{-2}$ for mm2-line. The corresponding abundances of methanol relative to H_2 can be calculated by using the H_2 column density derived by Beuther et al. (2007a) from the BCD configuration data. The methanol abundance of mm2 corresponds to 6×10^{-9} , a value closer to the ones derived towards the inner regions of low-mass protostars (e.g., Maret et al. 2005), than to values found in high-mass protostars (Menten et al. 1986, 1988). In Sect. 3.2, we noticed that, given the separation between mm2 and mm2-line, at least part of the emission of mm2 could come from the offset position. Therefore, the CH_3OH column density derived for mm2 should be regarded as an upper limit to its true value.

An upper limit to H_2 column density of mm2-line can be computed from the continuum emission at 1.3 mm, $N \sim 5 \times 10^{22} \text{ cm}^{-2}$ at 60 K. This results in an abundance of 1×10^{-7} for methanol, which is a factor of 17 higher than on mm2. However, a different dust temperature would result in different values for N_{H_2} and $X_{\text{CH}_3\text{OH}}$. The enhancement of methanol is usually ascribed to evaporation of icy grain mantles in the vicinity of warm embedded sources, e.g. hot cores, or to desorption of grain mantles in shocks associated to molecular outflows (e.g., Bachiller et al. 1995). Since no embedded sources are detected in the continuum emission at this position down to an upper limit of $0.08 M_{\odot}$, it seems likely that the molecular emission associated with mm2-line is related to the outflow activity of the region.

In the case of mm2, and mm2-line, the temperatures derived from methanol are comparable to those adopted by Beuther et al. (2007a) for the analysis of the continuum emission; therefore, only one value for the methanol abundance is given at this position.

Source mm3: as listed in Table 3, only molecular transitions from the ground state, and with upper energies of less than 70 K are detected toward mm3. Since all the lines detected toward this core are seen in absorption due to missing fluxes, with emission only in the $5_0 \rightarrow 4_0\text{-A}$ and $5_{-1} \rightarrow 4_{-1}\text{-E}$ transitions on top of the negative features, only a qualitative analysis of the data is possible. We ran LVG models for several temperatures and densities, to find the range of parameters compatible with our observations. The detection of the $5_{\pm 2} \rightarrow 4_{\pm 2}\text{-E}$ lines, and the non detection of the higher k transitions constrain the H_2 density to the range $\sim 10^5\text{--}10^6 \text{ cm}^{-3}$, while the tentative detection of the $k = 0\text{-A}$ and $k = -1\text{-E}$ lines in the $7_k \rightarrow 6_k$ band, but not of the other transitions, sets an upper limit to the temperature of 30–40 K.

4.4. Uncertainties on the physical parameters of the gas

Error ranges for the various parameters can be estimated by a χ^2 analysis, although this can only give errors within the assumptions of the model. It cannot assess errors due to the LTE and LVG assumptions and to the treatment of the gas as consisting of a finite number of non-interacting components of homogeneous conditions. As for the LTE assumption, densities in hot cores usually are in a range which makes it reasonable.

The analysis of CH_3CN and CH_3OH infers a source size of $\sim 0.2''$ for the gas responsible of the emission of the two velocity components found toward mm1a. This value is relatively well constrained by the CH_3CN band, which shows optically thick and thin lines, and by the non detection of $\text{CH}_3^{13}\text{CN}$. Since this result is in agreement with the size of the linear structure found from the fit of the positions of the velocity channels of methanol (see Fig. 7a), we fixed the source size to this value, and derived confidence levels for the estimates of the temperatures and column densities. However, one should remember that for optical thin lines, like the $v_t = 1$ CH_3OH transitions, the source

size and column density are degenerate parameters, and the estimates of the column densities would change, if the source size were different than our assumption. For CH₃OH toward mm1a, since these data were taken with a beam of $\sim 0.7''$ and we assumed a size of $0.15''$ in the calculations, the CH₃OH column density can only be a factor of 10 smaller than indicated by our results. For a source size of $0.15''$, good fits to the data are found also for lower temperatures, but higher column densities. For $T \sim 100$ K the model requires column densities of $\geq 10^{19}$ cm⁻², which would correspond to very high abundances relative to H₂ for such temperatures ($X_{\text{CH}_3\text{OH}} \geq 10^{-5}$). For temperatures higher than 150 K, the methanol column density is confined to the interval $4 \times 10^{17} - 2 \times 10^{18}$ cm⁻². A lower limit to the kinetic temperature is found at ~ 75 K, where the torsionally excited lines of methanol are not anymore efficiently pumped.

Similarly, the column density of SO₂ on mm1, and of CH₃OH on mm2 and mm2-line would increase if they were constrained to a region smaller in size than the value used in the calculation. For example, the column density of SO₂ would increase of one order of magnitude by using a source size of $0.2''$ as derived from the analysis of CH₃CN and CH₃OH.

The 3σ confidence levels derived for each parameter from the χ^2 analysis are given in Table 5, together with their best fit values.

5. Various stages of star formation

The analysis of the spectral line emission in IRAS 05358 reveals four dust condensations with a maximum projected distance of 18 000 AU. At least three of them show signs of active star formation. The core mm1a appears to be the most evolved source of the region, associated with a hypercompact HII region, and class II methanol masers. Beuther et al. (2007a) derived the Lyman continuum flux of mm1a corresponding to a B1 ZAMS star of $13 M_{\odot}$, and a large reservoir of accreting material ($\sim 10 M_{\odot}$). However, this estimate is obtained from relatively low resolution data, where the cores mm1a and mm1b are not spatially resolved. From high resolution data, which are however affected by missing fluxes, the estimate to the mass of mm1a is $1 M_{\odot}$, and $0.6 M_{\odot}$ for mm1b. Our observations suggest that mm1a also harbours a candidate circumstellar disk. A rough estimate of the luminosity of mm1a can be derived through the Stefan-Boltzmann formula, assuming a radius of 180 AU, and a temperature of 220 K. By adding the values for the two components, the total luminosity of mm1a is $L \sim 6000 L_{\odot}$, in agreement with the luminosity of $10^{3.72} L_{\odot}$ of a B1 ZAMS star (Panagia 1973). Since the total luminosity of the cluster is $6300 L_{\odot}$, this result supports the interpretation that mm1a is the main powerhouse of the region.

Viti et al. (2004) derived the abundances of several molecules in the gas phase, as function of the age, and of the mass of the heating central object. The abundances of CH₃OH, CH₃CN, and SO₂ of mm1a are in agreement with a $15 M_{\odot}$ star of approximately $10^{4.6}$ yr, although the best fit value for the column density of CH₃OH is higher than the theoretical values, but still consistent with the models within the uncertainties of the fit. Decreasing the mass of the heating source in the models results in increasing its age. The value of $10^{4.6}$ yr is in very good agreement with the value obtained by Beuther et al. (2002a) for the dynamical timescale of the molecular outflows originating from the vicinity of mm1 ($t \sim 37\,000$ yr).

The physical parameters of the gas derived from our analysis, (temperature and abundances) are similar to hot cores, thus implying that mm1a has already reached this evolutionary stage.

However, its molecular spectrum differs from the one of typical massive hot cores. Beuther et al. (2007b) studied the hot core in G29.96-0.02 ($L \sim 9 \times 10^4 L_{\odot}$, Olmi et al. 2003) with the SMA, with the same frequency setup we used for our SMA observations. Although the linear resolution reached for G29.96 is comparable to ours, the spectrum of G29.96 shows stronger methanol lines than IRAS 05358+3543 and higher excitation transitions; moreover, molecular species which are detected in G29.96 are not in our dataset. The same is found when comparing our observations with Orion-KL ($L \sim 10^5 L_{\odot}$), even with the poor angular resolution of the CSO telescope (Schilke et al. 1997). Possible explanations for these differences are that mm1a is indeed *a*) in an earlier evolutionary stage than the other two sources, at the beginning of the hot core phase, and will eventually reach their chemical richness; or *b*) hosts a less luminous hot core, which will never produce the rich chemistry of G29.96-0.02 or Orion-KL. Both interpretations render mm1a an interesting source, since they collocate it in a different region of the age-luminosity plane of hot cores, which still has not received much attention. Studies of large samples of hot cores at the same linear resolution, and with the same frequency setups (similar to that of Beuther 2007, but on a larger sample of sources) are necessary to better understand this evolutionary phase of star formation. Particularly interesting is the comparison with observations of hot cores in the vicinity of low- and intermediate-mass protostars, which could clarify whether the poorness of the chemistry in IRAS 05358+3543 is due to its age or it is rather an intrinsic property of less luminous hot cores.

Although the mm-wavelength thermal continuum emission of mm1b is similar in intensity and extent to that of mm1a, even if not as strong, mm1b is not associated with any cm continuum emission down to a threshold of 1 mJy, while mm1a is. Moreover, the molecular spectrum of mm1b seems very different from that of mm1a. Of all the species we observed, only C³⁴S is clearly found in mm1b. This is not a bias of our observations as other observations confirm our results. Class II methanol masers and a mid-IR source are detected only towards mm1a, hence confirming the different nature of the two cores. The core mm1b could be at an earlier stage of evolution, when the heating from the central star still has not produced any complex chemistry, nor formed a hypercompact HII region.

The region around mm2 represents a challenge for the interpretation of the continuum emission (Beuther et al. 2007a), as well as for the spectral data. Several sub-sources are identified around the main dust condensation, which are probably caused by the interaction of molecular outflows with the molecular cloud. Their total mass corresponds to $5 M_{\odot}$. The molecular emission associated with the dust core does not show any sign of highly excited lines, but points out at a warm ($T \sim 60$ K), dense ($n > 6 \times 10^6$ cm⁻³) gas with a methanol abundance of $\sim 7 \times 10^{-9}$. The $X_{\text{CH}_3\text{OH}}$ of mm2 is more similar to the values derived in star forming regions of lower mass than to high-mass young stellar objects. Given the total mass of the region, and the low abundance of methanol, we speculate that mm2 is a low-intermediate mass protostar. However, the spatial resolution of our data does not allow us to verify whether or not at least part of the emission from mm2 is indeed not coming from mm2-line.

The coldest and least active core of the region is the dust condensation mm3. Its mm continuum emission shows that mm3 is a compact, unresolved source even at the highest resolution reached by our observations (Beuther et al. 2007a). No compact molecular emission is detected from this core, but all the lines observed toward it are seen as negative features due to the filtering out of large structures of the data. The analysis of the

spectral energy distribution (Beuther et al. 2007a), and of the gas around the core confirm that mm3 is a dense ($n > 10^5 \text{ cm}^{-3}$), cold ($T < 40 \text{ K}$) condensation, surrounded by a large reservoir of accreting material ($M \sim 19 M_{\odot}$, Beuther et al. 2007a). The extended, flat distribution of molecules like CH_3OH , C^{34}S and H^{13}CO^+ , with no trace of the structure seen in the dust continuum emission, is reminiscent of low-mass starless cores, where C-bearing molecules are freeze-out onto the grain mantles in a cold and dense environments (e.g., Caselli et al. 1999). Could mm3 be a massive starless core? Massive starless cores can be found in the vicinity of active sites of massive star-formation, and should be quiescent displaying no signposts of star formation. Its properties suggest that mm3 is indeed a massive cold core in a very early evolutionary stage. However, with the observations we currently have we cannot exclude that star formation have already started in this core. In particular, we cannot exclude that mm3 is the driving source of one of the outflows detected in the region.

6. Summary

Our new interferometric data resolve at least four cores in the high-mass protocluster IRAS 05358+3543. By analysing the molecular spectrum of each condensations, we characterised the properties of the gas surrounding it. Our main results are summarised in the following:

- the main powerhouse of the region, mm1a, harbours a hot core with $T \sim 220 \text{ K}$, and the central heating source has a chemical timescale of $10^{4.6} \text{ yr}$. Our data suggest that mm1a might host a massive circumstellar disk;
- although the properties of the mm continuum emission of mm1b are very similar to the one of mm1a, the two sources differ significantly in the cm and mid-infrared spectrum. This core could be in an earlier stage of star formation than mm1a, since no molecular emission is detected toward it, with the only exception of the $5 \rightarrow 4 \text{ C}^{34}\text{S}$ transition;
- given the low abundance of methanol, mm2 could be a low-intermediate mass protostar;
- strong emission is detected in several molecular species to the north-west of mm2, at a position where no continuum emission is detected. We suggest that this is caused by the interaction of the outflows with the ambient molecular cloud;
- the least active source, mm3, could be a starless massive core, since it is cold ($T < 20 \text{ K}$), with a large reservoir of accreting material ($M \sim 19 M_{\odot}$), but no molecular emission peaks on it.

Acknowledgements. We would like to thank Jan Martin Winters and Roberto Neri for their helpful support during the reduction of the PdBI data, and Gabriel Paubert for performing the IRAM 30 m observations in service mode. We thank Vincent Minier for providing us with the positions of the velocity channels of the 6.7 GHz methanol maser line. H.B. acknowledges financial support by the Emmy-Noether-Program of the Deutsche Forschungsgemeinschaft (DFG, grant BE2578).

References

Bachiller, R., Liechti, S., Walmsley, C. M., & Colomer, F. 1995, *A&A*, 295, L51
 Beckwith, S. V. W., & Sargent, A. I. 1993, *ApJ*, 402, 280
 Beuther, H. 2007, in *IAU Symp.*, 237, 148
 Beuther, H., Schilke, P., Gueth, F., et al. 2002a, *A&A*, 387, 931

Beuther, H., Schilke, P., Menten, K. M., et al. 2002b, *ApJ*, 566, 945
 Beuther, H., Schilke, P., Sridharan, T. K., et al. 2002c, *A&A*, 383, 892
 Beuther, H., Walsh, A., Schilke, P., et al. 2002d, *A&A*, 390, 289
 Beuther, H., Zhang, Q., Sridharan, T. K., & Chen, Y. 2005, *ApJ*, 628, 800
 Beuther, H., Leurini, S., Schilke, P., et al. 2007a, *A&A*, 466, 1065
 Beuther, H., Zhang, Q., Bergin, E. A., et al. 2007b, *A&A*, 468, 1045
 Carroll, T. J., & Goldsmith, P. F. 1981, *ApJ*, 245, 891
 Caselli, P., Walmsley, C. M., Tafalla, M., Dore, L., & Myers, P. C. 1999, *ApJ*, 523, L165
 Cesaroni, R., Felli, M., Testi, L., Walmsley, C. M., & Olmi, L. 1997, *A&A*, 325, 725
 Cesaroni, R., Felli, M., Jenness, T., et al. 1999, *A&A*, 345, 949
 Cesaroni, R., Neri, R., Olmi, L., et al. 2005, *A&A*, 434, 1039
 Cesaroni, R., Galli, D., Lodato, G., Walmsley, C. M., & Zhang, Q. 2007, in *Protostars and Planets V*, ed. B. Reipurth, D. Jewitt, & K. Keil, 197
 Chen, H.-R., Welch, W. J., Wilner, D. J., & Sutton, E. C. 2006, *ApJ*, 639, 975
 Comito, C., Schilke, P., Phillips, T. G., et al. 2005, *ApJS*, 156, 127
 Faúndez, S., Bronfman, L., Garay, G., et al. 2004, *A&A*, 426, 97
 Fuller, G. A., Williams, S. J., & Sridharan, T. K. 2005, *A&A*, 442, 949
 Hatchell, J., Thompson, M. A., Millar, T. J., & MacDonal, G. H. 1998, *A&AS*, 133, 29
 Hatchell, J., Fuller, G. A., Millar, T. J., Thompson, M. A., & Macdonald, G. H. 2000, *A&A*, 357, 637
 Hunter, T. R., Brogan, C. L., Megeath, S. T., et al. 2006, *ApJ*, 649, 888
 Leurini, S., Schilke, P., Menten, K. M., et al. 2004, *A&A*, 422, 573
 Leurini, S., Schilke, P., Wyrowski, F., & Menten, K. M. 2007, *A&A*, 466, 215
 Longmore, S. N., Burton, M. G., Minier, V., & Walsh, A. J. 2006, *MNRAS*, 369, 1196
 Müller, H. S. P., Thorwirth, S., Roth, D. A., & Winnewisser, G. 2001, *A&A*, 370, L49
 Maret, S., Ceccarelli, C., Tielens, A. G. G. M., et al. 2005, *A&A*, 442, 527
 Megeath, S. T., Wilson, T. L., & Corbin, M. R. 2005, *ApJ*, 622, L141
 Menten, K. M. 1991, *ApJ*, 380, L75
 Menten, K. M., Walmsley, C. M., Henkel, C., & Wilson, T. L. 1986, *A&A*, 157, 318
 Menten, K. M., Walmsley, C. M., Henkel, C., & Wilson, T. L. 1988, *A&A*, 198, 253
 Minier, V., Booth, R. S., & Conway, J. E. 2000, *A&A*, 362, 1093
 Molinari, S., Brand, J., Cesaroni, R., & Palla, F. 1996, *A&A*, 308, 573
 Molinari, S., Brand, J., Cesaroni, R., Palla, F., & Palumbo, G. G. C. 1998, *A&A*, 336, 339
 Molinari, S., Brand, J., Cesaroni, R., & Palla, F. 2000, *A&A*, 355, 617
 Olmi, L., & Cesaroni, R. 1999, *A&A*, 352, 266
 Olmi, L., Cesaroni, R., Hofner, P., et al. 2003, *A&A*, 407, 225
 Panagia, N. 1973, *AJ*, 78, 929
 Pickett, H. M., Poynter, R. L., Cohen, E. A., et al. 1998, *J. Quant. Spectrosc. Radiat. Transf.*, 60
 Sault, R. J., Teuben, P. J., & Wright, M. C. H. 1995, in *Astronomical Data Analysis Software and Systems IV*, ASP Conf. Ser., 77, 433
 Schilke, P., Groesbeck, T. D., Blake, G. A., & Phillips, T. G. 1997, *ApJS*, 108, 301
 Schuster, K.-F., Boucher, C., Brunswig, W., et al. 2004, *A&A*, 423, 1171
 Shepherd, D. S., Yu, K. C., Bally, J., & Testi, L. 2000, *ApJ*, 535, 833
 Snell, R. L., Dickman, R. L., & Huang, Y.-L. 1990, *ApJ*, 352, 139
 Sridharan, T. K., Beuther, H., Schilke, P., Menten, K. M., & Wyrowski, F. 2002, *ApJ*, 566, 931
 Tofani, G., Felli, M., Taylor, G. B., & Hunter, T. R. 1995, *A&AS*, 112, 299
 Viti, S., Collings, M. P., Dever, J. W., McCoustra, M. R. S., & Williams, D. A. 2004, *MNRAS*, 354, 1141
 Walsh, A. J., Hyland, A. R., Robinson, G., & Burton, M. G. 1997, *MNRAS*, 291, 261
 Walsh, A. J., Burton, M. G., Hyland, A. R., & Robinson, G. 1998, *MNRAS*, 301, 640
 Walsh, A. J., Burton, M. G., Hyland, A. R., & Robinson, G. 1999, *MNRAS*, 309, 905
 Weigelt, G., Balega, Y., Preibisch, T., et al. 1999, *A&A*, 347, L15
 Williams, S. J., Fuller, G. A., & Sridharan, T. K. 2004, *A&A*, 417, 115
 Williams, S. J., Fuller, G. A., & Sridharan, T. K. 2005, *A&A*, 434, 257
 Wyrowski, F., Schilke, P., Walmsley, C. M., & Menten, K. M. 1999, *ApJ*, 514, L43
 Zhang, Q., Hunter, T. R., Brand, J., et al. 2001, *ApJ*, 552, L167
 Zhang, Q., Hunter, T. R., Brand, J., et al. 2005, *ApJ*, 625, 864
 Zhang, Q., Hunter, T. R., Beuther, H., et al. 2007, *ApJ*, 658, 1152